Nonresonant excess photon detachment of negative hydrogen ions

M. S. Gulley,[1] Xin Miao Zhao,[1] H. C. Bryant,[2] Charlie E. M. Strauss,[1] David J. Funk,[1] A. Stintz,[2] D. C. Rislove,[2] G. A. Kyrala,[1] W. B. Ingalls,[1] and W. A. Miller[2]

[1]*Los Alamos National Laboratory, P.O. Box 1663, Los Alamos, New Mexico 87545*

[2] *Department of Physics and Astronomy, University of New Mexico, Albuquerque, New Mexico 87131*

(Received 21 May 1999; revised manuscript received 12 August 1999)

One-photon detachment and two-photon nonresonant excess photon detachment of electrons from the H^- ion (outer-electron binding energy = 0.7542 eV) are observed with 1.165 eV laser pulses from a Nd:YAG laser (where YAG denotes yttrium aluminum garnet). A Penning ion source produces a pulsed 8 μA, 35 keV H^- beam that intersects a laser beam cylindrically focused down to a 17 μm full width at half maximum waist in the ion beam direction, creating a high-intensity interaction region with peak intensities of up to 10^{11} W/cm^2. The interaction time is 7 ps. The detached electrons are detected by a time-of-flight apparatus enabling us to detect a very small two-photon signal in the presence of a very large signal from single photon detachments. By rotating the linear polarization angle, we study the angular distribution of the electrons for both one- and two-photon detachments. The spectra are modeled to determine the asymmetry parameters and one- and two-photon cross sections. We find β_2 to be $2.54+0.44/-0.60$ and β_4 to be $2.29+0.07/-0.31$, corresponding to a D state of $89+3/-12\%$ of the S wave and D wave detachments for the two-photon results. The relative phase angle between the S and D amplitudes is measured to be less than 59°. The measured cross sections are found to be consistent with theoretical predictions. The one-photon photodetachment cross section is measured to be $(3.6\pm1.7)\times10^{-17}$ cm^2. The two-photon photodetachment generalized cross section is $(1.3\pm0.5)\times10^{-48}$ cm^4 sec, consistent with theoretical calculations of the cross section. The three-photon generalized cross section is less than 4.4×10^{-79} cm^6 sec^2. [S1050-2947(99)02812-7]

PACS number(s): 32.80.Rm, 32.80.Gc, 32.80.Wr, 32.90.+a

I. INTRODUCTION TO THE PHYSICAL SYSTEM

The negative hydrogen ion (H^-) is important in the development of three-body quantum mechanics. This fundamental bound three-body Coulombic system has no singly excited Rydberg levels, and, consequently, differs from most other atomic systems in its electron photoejection dynamics. The early successful picture of H^- by Bethe [1], with the polarization of the core hydrogen atom providing the binding potential for the second electron, demonstrated that H^- is an ideal case upon which to build approximation methods for two-electron systems and for the study of electron correlation effects. The detachment energy threshold (E_b) for H^- is only 0.7542 eV [2], making it easy experimentally to detach the electron. The broadly peaked absorption continuum is featureless below the onset of detachment resonances near 11 eV. In studies at photon energies of 1.165 eV, there will be no competing resonant processes for photon multiplicities below 9 or 10. An earlier paper on this work has been published [3]; in this paper we provide further details and analysis of this study.

We use the description ''excess-photon detachment'' (EPD) to describe the detachment of an electron from the negative ion with more than the required minimum number of photons (refer to Fig. 1). Previous multiphoton detachment measurements on H^- with laser energies below the binding energy were not sensitive to the EPD process [4]. Prior to the present work, EPD in H^- had been reported on only the two-photon $^1D^e$ resonance near 11.2 eV below the $n=2$ threshold [5]. The first observations of EPD used photons with energies well below the ion binding energy [6,7]. Multiphoton studies using photons with energies in excess of the binding energy are hampered by the strong one-photon detachment. Previously, the absorption of a second photon in this regime was observed only when enhanced by an intermediate ''window'' resonance [8] or final-state resonance [5]. This work describes the observation of EPD with a photon energy above the binding energy, without resonance enhancement, in the negative hydrogen ion, H^-. In this study, we report nonresonant EPD in the negative hydrogen ion when subjected to an intense beam from the Nd:YAG (yttrium aluminum garnet) fundamental mode with $h\nu$ of 1.165 eV. The focused photon beam is directed at 90° to the ion beam. The interaction time (about 7 ps) is determined by the transit time of the ions through the laser beam. We have established the feasibility of using slower beams (35 keV) combined with multiphoton techniques, to probe the structure of ions in a way that complements the previous work at LANCSE (formerly LAMPF) [4] at 800 MeV. With slower

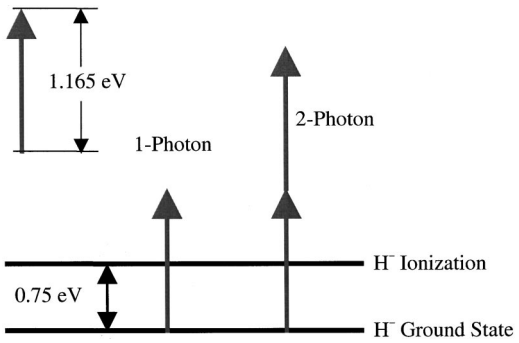

FIG. 1. Schematic diagram of the energy levels in H^- and the one- and two-photon detachments.

beams, although we do not have the advantage of large Doppler effects and motional electric fields, we have gained the ability to measure the energies of the detached electrons with enough resolution to sort out final states. We have demonstrated the basic multiphoton interaction in H^- using nonresonant EPD, with no stepping stones whatsoever.

The nonresonant two-photon process has been the topic of a theoretical study by Collins and Merts [9]. The multiphoton studies of Laughlin and Chu [10] as well as Liu, Gao, and Starace [11], are also relevant. Recently, Telnov and Chu have specifically addressed the question of angular distribution of detached electrons under conditions in the range of our measurements [12]. Nikolopoulos and Lambropoulos [13] have also performed calculations of two- and three-photon above-threshold ionization partial wave amplitudes and phase shifts for H^-. Sánchez, Bachau, and Martín [14] recently calculated detachment rates and angular distributions for H^-.

II. KINEMATICS

Two aspects of photodetachment of H^- can be experimentally investigated using our apparatus. First, the center-of-mass angular distribution of electrons is inferred by modeling the time-of-flight distribution of the raw data. The angular distribution (through conservation of momentum) tells us into which final states the electrons are ejected. Second, we are able to determine the cross sections for the one- and two-photon detachments by measurement of electron counting rates at known laser intensities.

After absorbing one or more photons from a laser beam, an electron is detached with velocity v_e from an ion in its rest frame. The velocity, v_e, is determined by the excess energy, T_e, the electron carries away from the system, given in the rest frame by $Nh\nu - E_b$, where N is the number of photons absorbed, $h\nu$ is the photon energy, and E_b is the electron binding energy. The ion is moving in the lab with beam velocity v. Treating the problem nonrelativistically, we find

$$\tan\theta_L = \frac{v_e \sin\theta_c}{v + v_e \cos\theta_c}, \tag{1}$$

where θ_L and θ_c are the ejection angles of the electron with respect to the beam direction in the lab and rest frames, respectively.

The kinetic energy of the electron in the lab frame, T, is given by

$$T = \frac{1}{2} m_e v_L^2 . \tag{2}$$

Equation (2) can be expressed in terms of center-of-mass quantities,

$$T = \frac{1}{2} m_e (v_e^2 + v^2 + 2 v_e v \cos\theta_c), \tag{3}$$

or

$$T = T_0 + T_e + 2\sqrt{T_0 T_e}\cos\theta, \tag{4}$$

where T_e is $\frac{1}{2} m_e v_e^2$ and T_0, $\frac{1}{2} m_e v^2$. By measuring the laboratory kinetic energy spectrum of the electrons for a constant T_e, we are in effect measuring the angular distribution of the detachments for a particular number of absorbed photons. Equation (4) demonstrates the kinematic amplification of this particular experimental procedure which allows us to extract the useful information. Notice that although T_e can be quite small, the angular-dependent part of T contains T_0 as well as T_e, which is especially important since the space-charge effects can be larger than T_e. Since the H^- beam is traveling at a velocity of 0.86% the speed of light, relativistic corrections to the kinematics are not significant.

A. Angular distributions

Since the initial state of the ion and the final state of the neutral atom are both S states, $[n\gamma + H^-(1\,^1S) \rightarrow H(1s) + e^-]$, the angular momentum of the absorbed photons must be disposed of in the orbital angular momentum between the ejected electrons and the neutral atom. In this case, as given by Blondel and Delsart [15], the electron angular distribution for linear polarization can be expanded with Legendre polynomials:

$$\frac{d\sigma}{d\Omega} = \frac{\sigma}{4\pi}\left(1 + \sum_{k=1}^{N} \beta_{2k} P_{2k}(\cos\theta)\right), \tag{5}$$

where σ is the total cross section, N is the number of absorbed photons, P_{2k} is the Legendre polynomial of order $2k$, θ is the angle between the ejection direction of the electron and the laser polarization, and β_{2k} is the asymmetry parameter of order $2k$. The dipole selection rule for the single-photon absorption requires a P wave angular distribution in the center-of-mass frame, while the two-photon absorption should produce a coherent superposition of an S and a D wave distribution. The branching ratio and phase angle of the scattering into the S and D processes arises through the photodetachment dynamics. The ejection angular distribution for the single photon with a linearly polarized laser corresponds to a P wave with $\beta_2 = 2$. In the case of two-photon absorption, the measured β_2 and β_4 tell us the branching ratio. We must obtain the angular distribution from the time-of-flight data; we start by relating the angular distribution to the energy distribution:

$$\frac{d\sigma}{dT} = \frac{d\sigma}{d\Omega_{\mathrm{CM}}}\frac{d\Omega_{\mathrm{CM}}}{dT}. \tag{6}$$

From Eq. (4), we find

$$\frac{dT}{d\Omega_{\mathrm{CM}}} = -\frac{1}{\pi}\sqrt{T_0 T_e}. \tag{7}$$

Because of azimuthal symmetry, the differential solid angle is

$$d\Omega_{\mathrm{CM}} = -2\pi d(\cos\theta_c). \tag{8}$$

For the final analysis, the differential time dependence of the cross section σ can be expressed as

$$\frac{d\sigma}{dt}=\frac{d\sigma}{dT}\frac{dT}{dt}. \tag{9}$$

The time derivative of the kinetic energy can be found from Eq. (2),

$$\frac{dT}{dt}=\frac{d(\frac{1}{2}m_e v_L^2)}{dt}=-\frac{m_e d^2}{t^3}, \tag{10}$$

where d is the distance the electron travels. Putting all of this together,

$$\frac{d\sigma}{dt}=\frac{d\sigma}{d\Omega_{\rm CM}}\frac{\pi}{2\sqrt{T_0 T_e}}\frac{m_e d^2}{t^3}. \tag{11}$$

Recalling Eq. (5) assuming linearly polarized light, we arrive at

$$\frac{d\sigma}{dt}=\frac{1}{\sqrt{T_0 T_e}}\frac{m_e d^2}{t^3}\frac{\sigma}{4}\left(1+\sum_{k=1}^{N}\beta_{2k}P_{2k}(\cos\theta)\right). \tag{12}$$

It is useful to see how the asymmetry parameters, β_{2k}, are related to quantities that are more intuitive, such as the relative presence of different states. In the two-photon case, Eq. (5) can be written

$$\frac{d\sigma}{d\Omega}=\frac{\sigma}{4\pi}[1+\beta_2 P_2(w)+\beta_4 P_4(w)], \tag{13}$$

where $w=\cos\theta$. We know physically that the two possibilities for the two-photon detachment are either an S wave, which can be represented by the spherical harmonic $Y_{00}(\theta)$, or a D wave, represented by $Y_{20}(\theta)$. The angular distribution can then be represented by a coherent mixture of these two possibilities:

$$\frac{d\sigma}{d\Omega}=\sigma[aY_{00}(\theta)+be^{i\phi}Y_{20}(\theta)]^2, \tag{14}$$

where $a^2+b^2=1$, and a, b, and ϕ are real. In this representation, a^2 and b^2 represent the fractions of S and D waves, respectively, and ϕ, the phase between the S and D waves. Comparison with Eq. (13) yields

$$\beta_4=\frac{18}{7}b^2 \tag{15}$$

and

$$\beta_2=2\sqrt{5}b\sqrt{1-b^2}\cos\phi+\frac{10}{7}b^2. \tag{16}$$

Thus, if the electrons are ejected purely in the D state, $b^2=1$ and $\beta_2=10/7$ and $\beta_4=18/7$.

Equation (5) describes the angular distribution with respect to the laser polarization. Since our observations are relative to the beam direction, we must transform Eq. (5). Let the angle between the H^- beam direction and the laser polarization direction be Φ as shown in Fig. 2. The cosine of the angle θ between the laser polarization and the electron ejection must be expressed in terms of Φ, θ_c, and χ, where the latter two angles are the polar and azimuthal angles of the electron's velocity vector in the center of mass, with a coordinate system whose z axis lies along the (horizontal) beam direction and whose y axis is vertical. Thus we can write

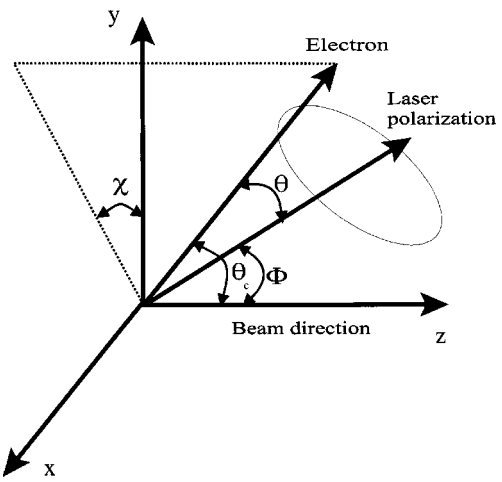

FIG. 2. Geometry when the laser is linearly polarized at an angle Φ with respect to the H^- beam direction. The electron is ejected at an angle θ with respect to the laser polarization.

$$\cos\theta=\cos\chi\sin\theta_c\sin\Phi+\cos\theta_c\cos\Phi. \tag{17}$$

Writing the Legendre polynomial as an expansion of spherical harmonics,

$$P_L(\cos\theta)=\frac{4\pi}{2L+1}\sum_M Y_{LM}(\theta_c,\chi)Y_{LM}(\Phi,0). \tag{18}$$

Averaging over χ, the spherical harmonics simplify to $P_L(\cos\theta_c)P_L(\cos\phi)$. Equation (5) becomes

$$\frac{d\sigma}{d\Omega}=\frac{\sigma}{4\pi}\left(1+\sum_{k=1}^{N}\beta_{2k}P_{2k}(\cos\theta_c)P_{2k}(\cos\Phi)\right). \tag{19}$$

The final form of the equation used to model the time-of-flight data is

$$\frac{d\sigma}{dt}=\frac{1}{\sqrt{T_0 T_e}}\frac{m_e d^2}{t^3}\frac{\sigma}{4}\left(1+\sum_{k=1}^{N}\beta_{2k}P_{2k}(\cos\theta_c)P_{2k}(\cos\Phi)\right). \tag{20}$$

Once the fit is made and the asymmetry parameters are determined, Eqs. (15) and (16) are used to determine the percentage of D wave and the phase angle between the S and D waves.

B. Ponderomotive potential

An electron detached by a high-intensity laser beam finds itself in a continuum state whose energy includes a ponderomotive (quiver) term arising from the electron's response to the ambient electromagnetic field. This time-averaged, classical ''ponderomotive potential energy'' is given by

$$E_p=\frac{r_e}{2\pi c}I\lambda^2, \tag{21}$$

where r_e is the classical radius of the electron, c is the speed of light, I is the laser power per unit area, and λ is the laser wavelength. In electron volts,

$$E_p = 9.337 \times 10^{-14} \lambda^2 I, \tag{22}$$

if I is measured in W/cm^2 and λ in μm.

This additional energy the electron must acquire in order to enter the continuum adds to its effective binding energy. However, in our case, with $\lambda = 1.064$ μm with I up to 10^{11} W/cm^2, the ponderomotive shift in energy is 0.01 eV. This energy difference translates into a time-of-flight difference of 0.1 ns, which is less than the resolution of our data-acquisition setup, and therefore is ignored.

C. One-photon cross section

In 1976, Broad and Reinhardt [16] used the multichannel J-matrix formulation of close-coupling theory to calculate the photodetachment cross section for H^-, yielding a one-photon cross section at a photon energy of 1.165 eV of about 3.510×10^{-17} cm^2. In order to extract the cross section from our results, we need to model the interaction of the H^- beam with the laser beam and determine what the counting rate should be, i.e., how many H^- ions are photodetached. Let the rate (R) be the product of the luminosity, L, and the cross section, σ,

$$R = L\sigma. \tag{23}$$

The luminosity is given [17] as

$$L(t) = (1 - \beta \cos\theta) \int dV F(\bar{r},t) n(\bar{r},t), \tag{24}$$

where θ is the angle between the laser beam and the particle beam, F is the photon flux density in photons per second per unit area, and n is the ion density in ions per unit volume. β is the usual relativistic velocity ratio and $\bar{r}$ is the ion beam spatial coordinate system.

The simplest case is to model both the ion beam and the laser pulse as uniform overlapping cylinders of radius a, in which the luminosity becomes

$$L = 16a^3(1 - \beta \cos\theta) nF/(3 \sin\alpha). \tag{25}$$

This simple model, however, is inadequate for accurately predicting our data for two reasons. First, our laser beam has a Gaussian intensity profile, and second, the intensity is high enough that our ion beam can be significantly attenuated. Let us consider an ion that has survived up to the point z in the laser pulse; the probability of detachment in the next interval dz, dP is given by

$$dP = -\sigma(E',F') F(x,y,z,t) \frac{1 - \beta \cos\theta}{\beta c} P(x,y,z,t) dz, \tag{26}$$

where the primed quantities are in the ion rest frame. Integrating Eq. (26) gives us the probability $P_s(x,y,z)$ for an ion to survive to a point x,y,z into the laser pulse:

$$P_s(x,y,z) = \exp\left\{ -\frac{1 - \beta \cos\theta}{\beta c} \times \int_{-\infty}^{z} dz' \sigma(E',F') F(x,y,z) \right\}. \tag{27}$$

The complement to the probability of survival is the detachment probability, $P_D(x,y,z)$, given by

$$P_D(x,y,z) = 1 - P_s(x,y,z). \tag{28}$$

We can now consider the instantaneous detachment rate per ion, $r_D(x,y,z,E')$, given by

$$r_D(z) \equiv \beta c \frac{\partial P_D}{\partial z} = \sigma(1 - \beta \cos\theta) F \times \exp\left[-\frac{1 - \beta \cos\theta}{\beta c} \int_{-\infty}^{z} dz' \sigma F \right]. \tag{29}$$

By integrating this rate up to point z, we can determine the total number of detachments. We now specifically consider the spatial and temporal structure of the laser pulse. We will approximate it to be Gaussian in both space and time, so the flux can be written as

$$F(\bar{r},t) = \frac{2N_\nu}{\pi^{3/2}\sqrt{2}\Delta_L \omega^2} \exp\left[\frac{-t^2}{2\Delta_L^2} \right] \exp\left[\frac{-2(x^2+y^2)}{\omega^2} \right], \tag{30}$$

where N_ν is the number of photons per laser pulse, ω is the laser beam waist, and Δ_L is the temporal standard deviation. We may now look at the spatial dependence of this relationship. The coordinate system for the ion pulse is (x,y,z), where z is the ion beam direction; the coordinate system for the laser pulse is $(\bar{x},\bar{y},\bar{z})$, where $\bar{z}$ is the laser beam direction. The intersection angle θ is the angle between the z and $\bar{z}$ axes. The laser spot obeys the relation

$$w^2(\bar{z}) = w_0^2 \left(1 + \frac{\bar{z}^2}{z_R^2} \right), \tag{31}$$

where z_R is the Rayleigh range, $\pi w^2/\lambda$. The transformation between frames is then

$$\bar{x} = -z \sin\theta + x \cos\theta,$$

$$\bar{y} = y,$$

$$\bar{z} = z \cos\theta + x \sin\theta.$$

So the spatial-dependent part of the laser flux can be written as

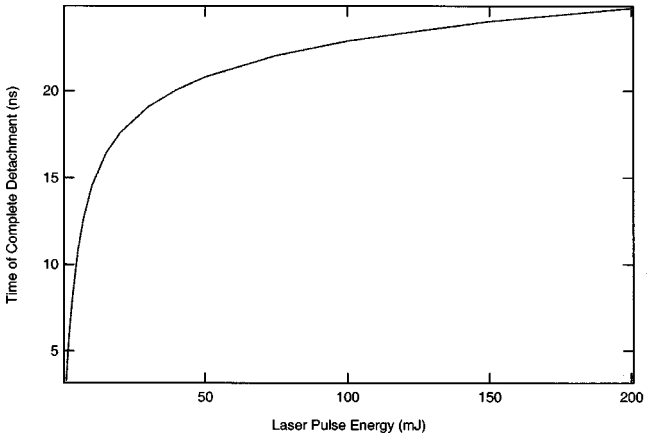

FIG. 3. Results of the model for one-photon detachment yields. The yield is given in terms of the duration of a bite out of the H^- beam equivalent to all of the events produced by the process.

$$F(\overline{r}) = \frac{2N_\nu}{w_0^2\left(1+\dfrac{(z\cos\theta + x\sin\theta)^2}{z_R^2}\right)} \times \exp\left\{\frac{-2(x\cos\theta - z\sin\theta)^2 + y^2}{w_0^2\left(1+\dfrac{(z\cos\theta + x\sin\theta)^2}{z_R^2}\right)}\right\}. \quad (32)$$

By integrating Eq. (29) using Eqs. (30) and 32 to model the temporal and spatial structure of the laser pulse, we can predict the yields of the different detachment processes as a function of the laser pulse energy. By fitting the yield curves to the experimental results, we are able to extract cross-section values. Figure 3 shows how the yield of the one-photon process depends on the laser energy,. At high laser energy the large depletion of the H^- pulse causes the yield to level off. The H^- beam is mostly depleted even before it reaches the highest intensity region of the laser pulse.

D. Two-photon cross section

Two recent calculations of the generalized cross section for the nonresonant two-photon process are by Liu, Gao, and Starace [11] and by Proulx and Shakeshaft [18]. The former did not calculate the cross section for photon energies higher than 0.65 eV, so we will need to compare to the latter results (these two calculations are consistent with each other at lower photon energies). There is also a new study by Nikolopoulos and Lambropoulos [13] that investigates both the *S* to *D* ratio and the photodetachment cross sections for the two- and three-photon events. In Fig. 4, we show our predicted yield for the two-photon process. By fitting this yield curve to the experimental yields, we extract the cross sections to compare to the theoretical models.

Figure 5 shows what the predicted photodetachment rate, as the ion penetrates the laser beam, looks like for the two-photon process. Here one can see that the detachment peaks before the H^- beam makes it to the center of the laser pulse, where the laser intensity is greatest. By this point, the one-photon process has depleted the H^- beam to the point where, even though the laser intensity is greater, there are not enough ions left for there to be a large two-photon photodetachment rate. The surviving fraction of the H^- beam is also shown.

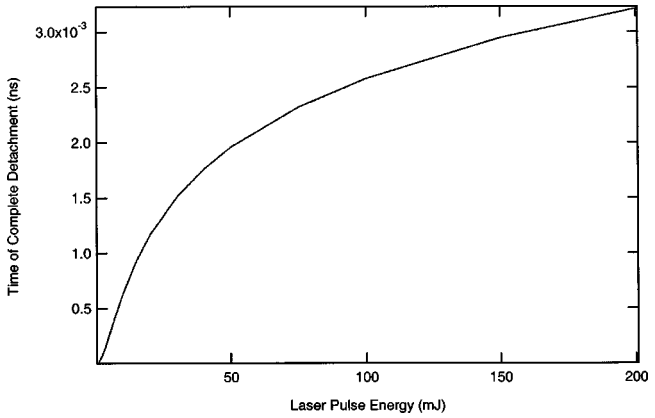

FIG. 4. Results of the model for two-photon detachment yields. The vertical axis represents the time the H^- beam is completely detached by two-photon events, as defined in the Fig. 3 caption.

E. Three-photon cross section

In a manner similar to the two-photon calculation, we can also calculate the yield of the three-photon process to extract a cross section. In this case, our experiment was not sensitive enough to detect the three-photon peak, so we will be able to estimate only an upper limit on the three-photon cross section. Figure 6 demonstrates the expected three-photon yield versus laser pulse energy.

III. EXPERIMENTAL METHOD

Our experimental goal was to measure the time-of-flight spectra of the electrons produced by two-photon detachments. These data are analyzed to determine the angular distribution and yield of the two-photon detachment. The principal experimental hindrance is single-photon detachment,

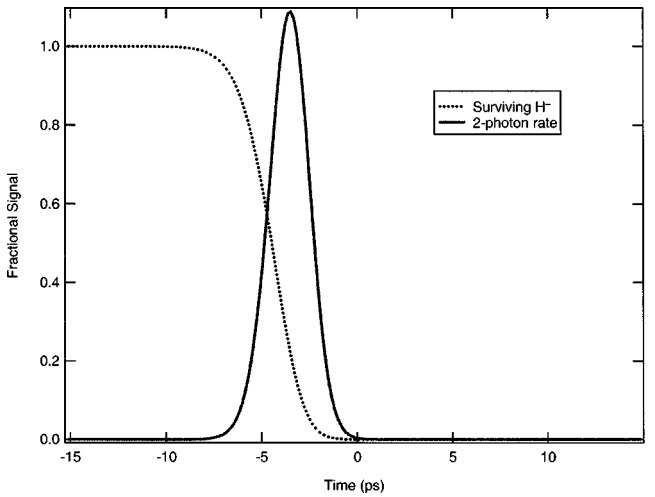

FIG. 5. This figure shows the shape of the two-photon detachment rate compared to the depletion of the H^- beam. Notice that the beam is substantially depleted by the time it reaches the peak of the Gaussian laser pulse (at time = 0). Thus, the two-photon detachment rate hits its maximum at an intermediate point.

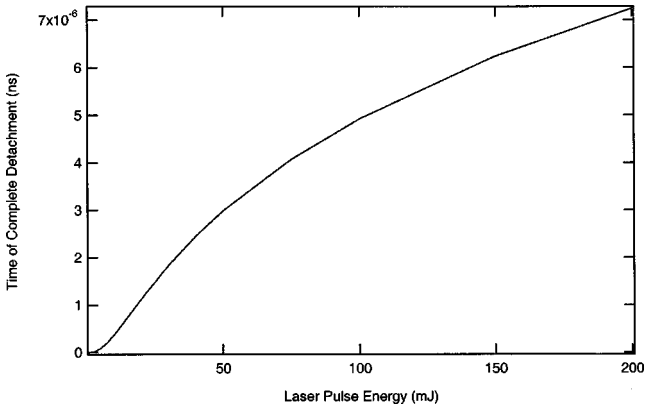

FIG. 6. Model of the three-photon detachment rate versus laser pulse energy. The vertical axis represents the time the H^- beam is completely detached by three-photon events, as defined in the Fig. 3 caption.

which depletes the ions before they can reach the intense field region where nonlinear two-photon processes occur appreciably. Nevertheless, we resolved two-photon EPD photoelectrons in the energy spectrum resulting from a fast high current ion beam [19] directed at 90° through a focused 11 ns pulsed laser beam. An alternative approach to produce an abrupt onset of the photon field intensity requires firing a picosecond laser [8] into a slow moving H^- beam, although this method is inherently less productive per laser pulse. Details of the experimental setup using a different laser arrangement are also discussed in Ref. [5]. The two main pieces of equipment for this experiment were an ion accelerator to produce a beam of H^- ions and a laser to produce a beam of photons. These two beams were made to intersect in an interaction chamber and the resulting detached electrons were guided by a magnetic bottle to a microchannel plate detector (MCP). The MCP signal was sent to an oscilloscope, averaged, and then sent to a computer to be recorded.

A. The H^- ion source: The ground test accelerator

The ground test accelerator (GTA), the centerpiece of the Neutral Particle Beam Program at Los Alamos [20], was stimulated by the successful demonstration of a neutral beam in space in July, 1989 [21], and required the development of high brightness H^- ion sources. The 4X H^- Penning ion source developed for the GTA provides a 46 mA peak H^- beam accelerated to 35 keV and pulsed at 5 Hz [22]. This beam was fed through our beam transport line into the interaction chamber.

B. The photon source: Nd:YAG laser

A Quanta Ray GCR-4 neodymium-doped yttrium aluminum garnet (Nd:YAG) laser provided the laser beam. In order to avoid transient spikes and hot spots due to multimode laser beams when modeling multiphoton processes [23,24], an injection-seeded Nd:YAG laser provided a single-mode pulse with a smooth, reproducible temporal profile with a full width at half maximum (FWHM) of approximately 11 ns. This laser provided photons at a wavelength of 1064 nm (1.165 eV), and produced pulses with an energy of up to 1 joule, at a repetition rate of 10 Hz. The laser beam was tightly focused by a cylindrical lens ($f=10$ cm) to a 17 μm (FWHM) thick photon sheet perpendicular to the ion beam direction. The sheet height (FWHM) was 2 mm, determined by another cylindrical lens ($f=25.4$ cm) placed 20.3 cm from the interaction region. Since the diameter of the ion beam was about 1 mm, this height assured complete overlap of the two beams. Traveling at 0.86% the speed of light, each ion transits the laser field in less than 7 ps. Since the H^- particles are traveling so much faster than the residual gas particles in the system, the photoelectrons from these background particles make minimal contributions to the signal of interest.

C. The optics system

The laser is designed to run optimally at a 10 Hz repetition rate, even though it can be operated at any rate between 0 and 30 Hz. The ion source runs at 5 Hz, so the simplest way to trigger the laser would have been to trigger it directly from the source trigger signal. However, to be able to run the laser optimally, we doubled the source trigger signal frequency to form a 10 Hz laser trigger. In this way we got the proper timing between the laser pulse and the ion pulse, although only alternate laser pulses were used.

The optical beam path contained primarily a $\lambda/2$ plate for rotating the linear polarization of the laser beam and two cylindrical lenses for focusing the laser. The first lens had a focal length of $+25.4$ cm and was placed 20.3 cm from the interaction region. It was oriented to focus in the vertical direction. This narrowed the 1 cm diameter beam down to about 2 mm in the interaction area. The second lens was a $+10.2$ cm focal length cylindrical lens placed to focus at the interaction region. This lens was oriented to focus the laser beam along the H^- beam direction of travel (z axis in Fig. 2). The focal region was designed to allow the H^- ions to reach areas of high laser intensity in the shortest possible time, so that two-photon processes can take place before the one-photon processes completely deplete the H^- beam.

The laser beam waist was measured by moving a razor blade through the beam waist and measuring the total signal in the one-photon peak versus razor edge position. The derivative of the total one-photon signal with distance transverse to the beam produces the Gaussian shape of the effective focal spot.

D. The interaction chamber

Figure 7 shows a schematic overview of the apparatus, including the beamline and interaction chamber. Figure 8 shows the details of the interaction chamber.

An aperture reduced the H^- flux extracted from the accelerator to 8 microamperes, and the beam was directed by an Einzel lens through a set of electrostatic deflection plates. These plates were tuned to deflect the H^- particles, but not H^0 or H^+, through the interaction region, making the beam as pure H^- as possible. The 5 Hz H^- beam pulses were nominally 500 ms in length. Since the laser pulse is only about 11 ns in duration, most of this beam goes only to increase the background pressure in the interaction region. For this reason an electrostatic chopper after the Einzel lens shortened the beam pulses to 100 ns duration. The H^- beam passed through the interaction region into a Faraday cup for

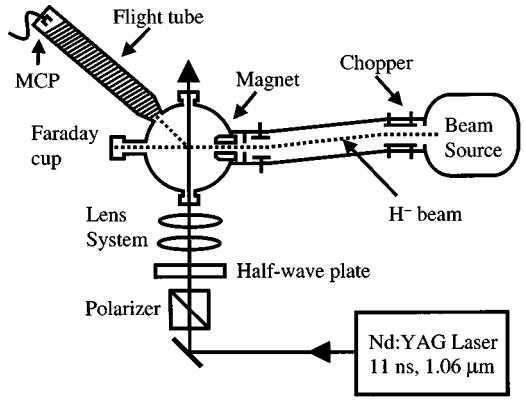

FIG. 7. Schematic overview of experimental apparatus.

measurement of the beam current. Immediately before the interaction region, the 1 mm diameter H^- beam passed through a cylindrical 5 mm hole along the symmetry axis, parallel to the field, of a cylindrical samarium-cobalt permanent magnet. This magnet, with a peak field of 2700 G, formed the entrance field to a magnetic bottle time-of-flight apparatus [25,26]. The laser beam intersects the H^- beam about 3 mm beyond the exit from the permanent magnet. Photodetached electrons are guided by the magnetic field lines from the permanent magnet into the solenoidal field of the time-of-flight tube.

E. Detection equipment

The laser and ion beams intersect near the maximum field of the permanent magnet. The magnetic field, as it diverges from the axis of symmetry of the magnet, adiabatically aligns and expands the photodetached electron trajectories into the throat of the time-of-flight (TOF) magnetic bottle. A microchannel plate (MCP) detector at the end of the meter-long solenoid flight tube time-resolves the photodetached electron pulses. A current coil trims out the earth's magnetic field transverse to the TOF tube. The signal is averaged for 1000 laser pulses using a digital oscilloscope with a time resolution of 2.5 ns. The instrumental response time, limited by the laser pulse width, space-charge repulsion, and non-ideal magnetic collimation, is found to be approximately 11 ns by convolving Eq. (20) to fit the one-photon detached electron TOF distribution. The MCP is a double-plate, or chevron, design. Each of the two stages or plates multiplies the electron signal by a factor of one thousand, giving a total gain of the electron signal of about one million. Each plate is kept at a potential of about 1000 V. The electrons detached from a 35 keV H^- beam have, not taking into account the excess energy imparted to them by the photons, an energy of 19 eV in the lab frame. This 19 eV is not enough to create the cascade of electrons in the front plate of the MCP; the front end of the front plate is therefore held at a positive potential of several hundred volts to accelerate the electrons at the last instant enough to create a detectable signal. The amplified electron current pulse then charges up a high-voltage capacitor circuit and the resulting voltage signal pulse is sent to an oscilloscope. The oscilloscope time sweep is triggered by a coincidence between a photodiode detecting the laser pulse and the trigger pulse from the H^- source. The oscilloscope then averages the electron signal over typically 1000 laser pulses, resulting in a raw time-of-flight spectrum.

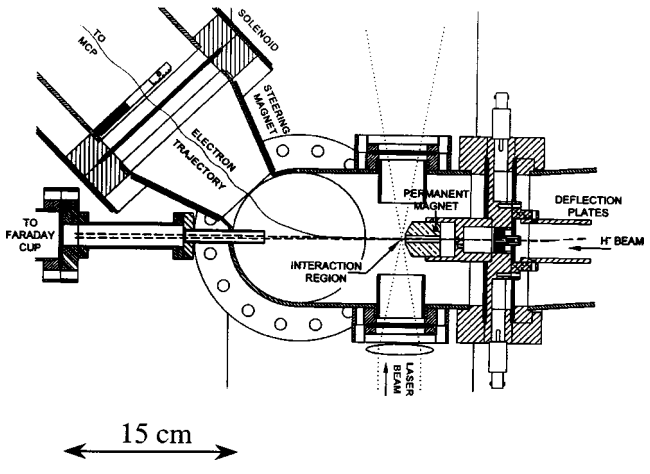

FIG. 8. Detailed design of the interaction chamber showing the second set of deflector plates, permanent magnet, interaction region, and the front end of the time-of-flight tube.

F. Data acquisition

The oscilloscope (LeCroy 9450A) is controlled by a personal computer using LabVIEW software. The software is written to allow the user to input the file name, the number of counts over which to average, and the time and voltage settings on the oscilloscope. Once activated, the program sets the oscilloscope to average the electron signal for the specified number of counts, and then collects the averaged TOF signal and places it in the user-specified file.

IV. DATA ANALYSIS

A. The data

In the ion rest frame, the photoejected electron distributions for a particular laser frequency and photon multiplicity are expected to be monoenergetic and cylindrically symmetric about the laser polarization axis. As discussed in Sec. II, the TOF spectrum of the photodetached electrons reflects their ion center-of-mass angular distribution. Consequently, the desired β_{2k} values which characterize the branching ratio and angular distribution can be inferred from the TOF spectrum. In principle, fitting the model to a single spectrum for a particular angle Φ, the angle of polarization of the laser beam with respect to the ion beam (zero degrees means the laser polarization is along the H^- beam direction) will suffice to determine the asymmetry parameters β_{2k}. In practice, we took data at different laser polarization angles Φ to be able to cross check the data. Φ is stepped through a sequence of values with a half-wave plate, and, at each value of Φ, the one- and two-photon detached electron TOF spectra are recorded. Figures 9(a) and 9(b) show typical arrival time distributions for several polarization angles for the one- and two-photon distributions. The one- and two-photon arrival time distributions overlap partially, so that only the leading edge of the two-photon signal is visible, as seen in Fig. 9(b). The rising signal at arrival times after 380 ns marks the onset of the overlap of the weak two-photon signal with the strong one-photon signal.

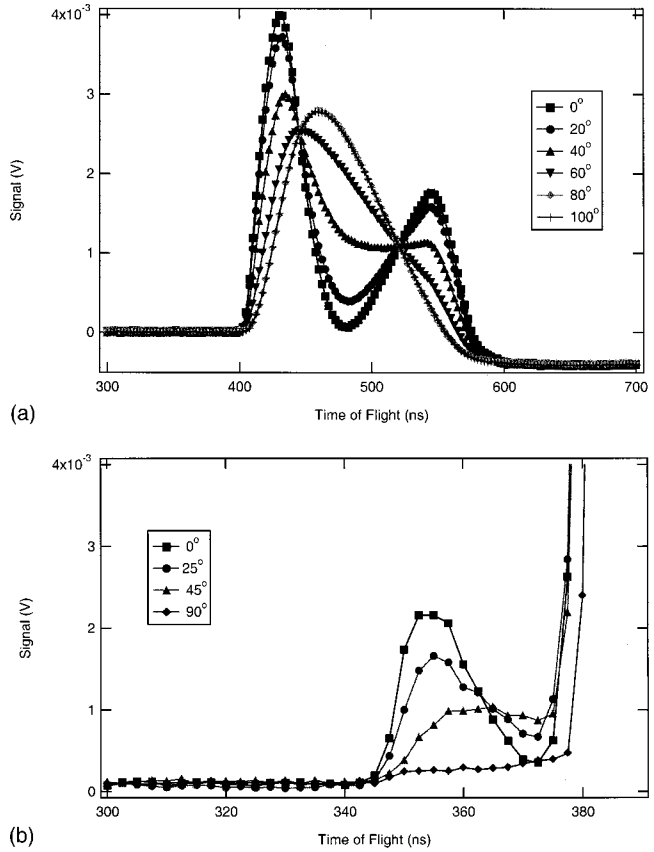

FIG. 9. Angular dependence of time-of-flight signal for (a) one-photon and (b) two-photon detached photoelectrons. The top plot in each case shows the height of the leading peak as a function of laser polarization angle. The lower plots show three typical electron arrival time distributions corresponding to three polarization angles. The solid line is the expected behavior for a pure P wave and D wave angular distribution for the one-and two-photon yield, respectively.

No new physics would be expected to arise from the shape of the one-photon spectrum, since the only appreciable possibility is for the electrons to be ejected in a P state, meaning that β_2 should be 2. The accuracy to which the data can be modeled by a β_2 of 2 with higher-order betas of 0 is a test of the accuracy of the dipole approximation in this case. We found that the best-fit value for β_2 is 1.96 ± 0.03, slightly below its expected theoretical value. Fits which included higher-order betas did not improve the confidence level of the fit and gave values of the higher-order asymmetry parameters that are consistent with zero. Telnov and Chu [12] performed a nonperturbative Floquet calculation of this system and included higher-order terms. For a laser intensity of 10^{11} W/cm^2, their value of β_4 for the one-photon detachment is -4.56×10^{-4}, smaller than our uncertainty in the values of the asymmetry parameters. Thus, the dipole approximation is sufficiently accurate to model our data. We were able to use the one-photon spectra to test the model that we use on the two-photon spectra. This turned out to not be as useful as we had originally hoped; important parameters, such as the time spread due to the laser pulse, are different between the one- and two-photon data. The two-photon signal is on the order of 1000 times smaller and is measurable only at higher laser intensities. Thus, there is a shorter period

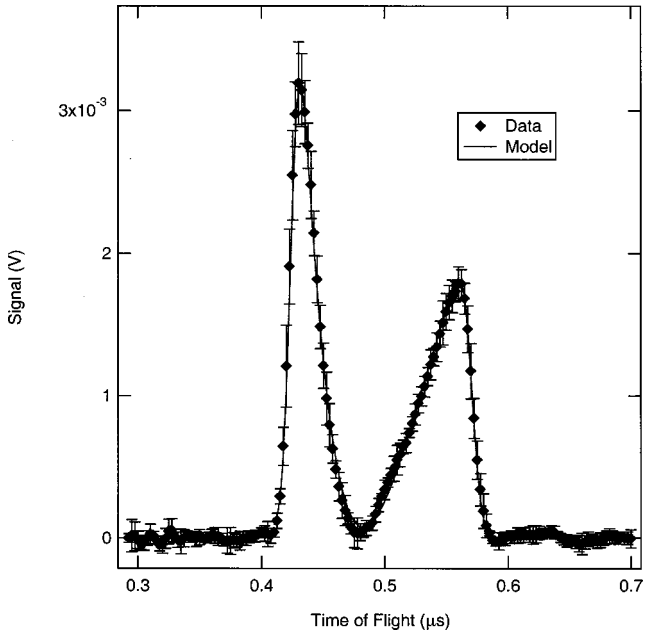

FIG. 10. One-photon time-of-flight spectrum with the best-fit model. To produce a spectrum with this little distortion of the low-energy side, both the laser power and H^- beam current had to be reduced to minimal levels. This fit establishes the essential validity of the dipole approximation for these conditions.

of time during which the laser pulse produces two-photon electrons. This also explains why, even though the width of the laser beam is about 11 ns FWHM, for the two-photon data the time spread is usually about 6.7 ns FWHM. For the one-photon data, the best fit is typically with a spread of 11 ns FWHM.

B. Time smear of the data

A model for the expected TOF structure was constructed by convolving into the electron arrival distribution at the MCP a Gaussian shape for the laser pulse, with a FWHM of 11 ns. Because of the need to model the smear in the data created by the laser temporal structure, it was beneficial to use a seeded laser in which the pulse was smoothed.

Figure 10 shows a one-photon time-of-flight spectrum and its best fit. It was difficult to get a good one-photon spectrum because the signal was strong enough to easily saturate the MCP. The distortion to the signal created by the RC time response of the MCP is accounted for in the analysis by convolving the time-spread signal with a dying exponential to represent the RC time constant. We eventually used an MCP in which the capacitor was external and easily changed. We experimented with different capacitance values to try to minimize the effect of the time constant. The effect is not as great on the two-photon signal since the visible portion arrives at the MCP for a small time period relative to the RC time constant.

The fitting routine can include spread of the time-of-flight distribution due to space-charge effects if so desired. However, space-charge effects seem to have no significant effect on the raw data spectra. Figure 11 is an example of how the pure D state model of the two-photon process looks. The three peaks in the spectrum come from the three high probability regions of the D orbital. Figure 12 shows a fit to the

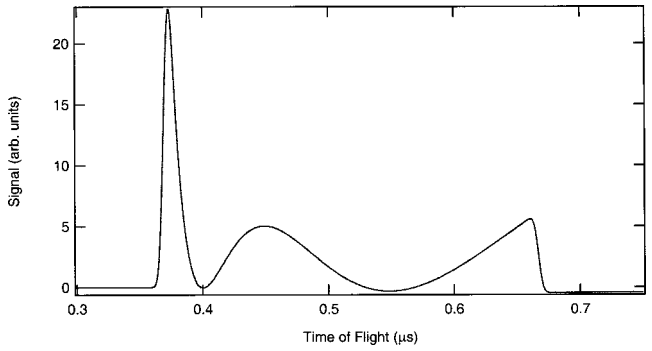

FIG. 11. Model of the two-photon time-of-flight spectrum at a laser polarization angle of zero.

data. Notice that we have access to only the front end of the two-photon signal, as the one-photon signal obscures most of the rest except for the low-energy end of the two-photon signal, which is too weak and temporally extended to be useful. The asymmetry parameters were the fitting parameters. A discussion of the fitting procedure can be found in [27].

C. Yields

We examine the dependence of the yield of the one- and two-photon processes on the laser power. The single-photon electron yield initially increases linearly with the laser irradiance and eventually saturates. Other studies attribute this nonquadratic behavior to quantum interference effects from multiple detachment channels [28,29], incomplete overlap of the laser focus and the ion cloud [30], and competition by other processes [24]. Since our electrons are generated predominantly in a single orbital angular momentum state (as discussed below), interference is a weak effect and our sheet focus geometry assures the overlap of the ion and laser beams. Our model indicates that the observed laser intensity dependence can be accounted for by the single-photon detachment, which depletes the ions before they can reach the peak laser power; indeed, despite the 7 ps transit time, essentially all two-photon events occur prior to the peak intensity of the laser focus. We emphasize that depletion does not represent a corruption of the measurement process; in particular, it should not affect the energy or angular distribution of the one- and two-photon photoelectrons.

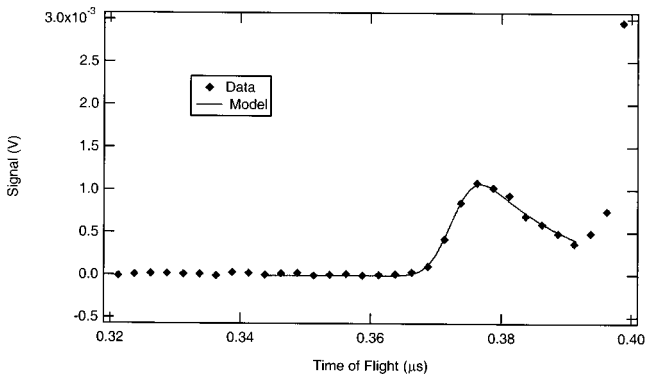

FIG. 12. Two-photon time-of-flight spectrum with the best-fit model.

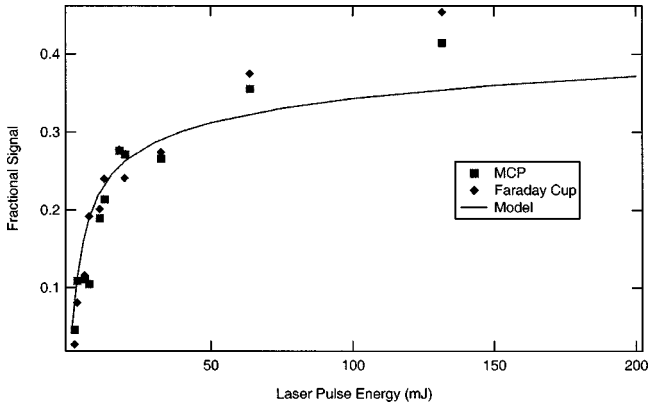

FIG. 13. The fraction of the H^- beam that undergoes one-photon detachments vs photon pulse energy, showing the comparison between the model and the final data.

D. Converting the data to useful yields

The raw data consist of signals in units of volts versus time from the oscilloscope that are not directly normalized or calibrated. The one-photon signal can be calibrated by use of the Faraday cup signal. The one-photon detachment signal is strong enough that a visible notch is seen in the Faraday cup spectrum, corresponding to the ions neutralized by this process. By normalizing the area of this notch to the area of the background signal, we can determine the fraction of the H^- beam photodetached. We also compare the area of the one-photon signal taken from the MCP to that from the Faraday cup. The tendancy at larger laser pulse energies for the MCP signal to be less than the Faraday cup signal is caused by the electron signal saturating the MCP, effectively decreasing its gain. This saturation can be seen in the shape of the time-of-flight spectrum. As the signal strength increases to the size where depletion of the MCP plates occur, the area under the low-energy side of the spectrum decreases.

The normalized one-photon signal can be compared to the yield predicted by integrating Eq. (29) and modeling the laser pulse. We adjust the cross-section parameter for the best fit. Our model is compared with the data in Fig. 13. There is a systematic overestimation of the yield at intermediate laser pulse energy values that we believe is due to nonoptimal alignment of the optics.

V. RESULTS AND CONCLUSIONS

We observed nonresonant EPD in H^- with the absorption of two photons of energy 1.165 eV. This regime is particularly interesting because it lies far above threshold [31], near the maximum [16] of the single-photon continuum, and the one- and two-photon energies are not near any intermediate or final resonances or features. Even though the one-photon absorption process severely depleted the ions penetrating to the most intense region of the laser focus, we observed nonresonant EPD from a two-photon absorption.

A. Branching ratios and phase angle between *S* and *D* waves

The asymmetry parameters are determined from fits to the TOF profiles. We find β_2 to be $2.54+0.44/-0.60$ and β_4 to be $2.29+0.07/-0.31$. The branching ratio of the *S* and *D* wave ejection processes is determined from the asymmetry

parameters. The process appears to branch 89% $+3/-12\%$ into the D wave. The final number is a weighted average [32] of the final set of results. The model predicts the phase angle, ϕ, as defined in Eq. (14) to be $25° \pm 34°$, that is, a phase angle of less than 59°. The uncertainty is due to systematic distortions of our signal inadequately accounted for in our model. For a light atom, where the interaction of the outgoing electron with the residual core is minimal, theoretical calculations using the plane-wave approximation have shown quantitative agreement with previous experiments [33]. In the plane-wave approximation [34,35], the relative phases of the different angular momentum (l) amplitudes differ by $\pi\Delta\lambda/2$, so that, in our case, the S and D wave channels should have an interference angle of π [35]. The Wigner law [36] predicts that near threshold the branching among processes of differing angular momentum will scale as $T_e^{l+1/2}$; as the excess energy increases, the fraction of population in the lower angular momentum states declines. Past studies [35,7] have shown good agreement with the Wigner law near threshold. If the law holds far from threshold, then it predicts very little S-state production [37]. Collins and Merts [9] (momentum-space method) as well as Telnov and Chu [12] (Floquet method) predict that, at the photon energy and laser intensities in our experiment, the D state dominates the two-photon detachment state; Telnov and Chu predict [12] greater than 90% D wave population. Our experimental results appear to confirm these theoretical predictions.

B. One-photon cross section

We modeled the one-photon yield versus laser energy and compared it to our data. We adjusted the one-photon cross section until we had a best fit: $(3.6 \pm 1.7) \times 10^{-17}$ cm^2. Figure 13 shows how the yield curves look for the data versus the model. The fit is best at the lower pulse energies. Our results are consistent with the predictions of Broad and Reinhardt [16], 3.58×10^{-17} cm^2 at our photon energy of 1.165 eV.

C. Two-photon cross section

Proulx and Shakeshaft give the detachment rate as being 25 800 (in atomic units of rate per I^2). This converts to a generalized cross section of 9×10^{-49} cm^4 sec. Nikolopoulos gives the $1S$ rate as being about 2500 and the $1D$ rate as about 30 000, which combined to give a generalized cross section of about 1.1×10^{-48} cm^4 sec. Our results gave a best fit of the data with a generalized cross section of $(1.3 \pm 0.5) \times 10^{-48}$ cm^4 sec. Our cross-section value is consistent with the theoretical predictions. The results of the model being fit to our best data runs are shown in Fig. 14.

D. Upper limit on three-photon cross section

We were unable to detect detachments from the three-photon process. However, from the size of the noise in the region of the spectrum where the three-photon signal should be, we can estimate an upper limit on what the cross section could be. We calculate the noise for one channel of our time-of-flight spectrum based on the noise in that region. We assume the noise is the upper limit to the three-photon signal and add the noise over all the channels in which we would expect to see the three-photon process. We compare this upper limit to the three-photon yield to the size of its two-photon counterpart on that spectrum to calibrate it. By adjusting the generalized three-photon cross section in the modeling program until it produces a yield equal to our upper-limit value, we get a limit on the generalized cross section for the three-photon process; it must be less than 4.4×10^{-79} cm^6 sec^2. Nikolopoulos and Lambropoulos [13] calculate the three-photon detachment rates to be about 3×10^6 for both the ^1P and the ^1F in atomic units of rate/I^3, giving a total rate of 6×10^6, which converts to a generalized cross section of 8×10^{-80} cm^6 sec^2, consistent with our estimate.

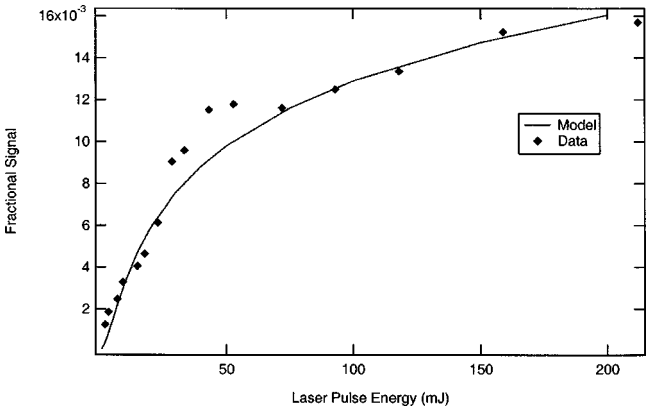

FIG. 14. Comparison of the model to the final data for the two-photon process.

E. Summary

We measured the photodetachment cross sections for the one- and two-photon photodetachment processes using photons of energy 1.165 eV. The one-photon cross section is $(3.6 \pm 1.7) \times 10^{-17}$ cm^2. The two-photon generalized cross section is $(1.3 \pm 0.5) \times 10^{-48}$ cm^4 sec. We find β_2 to be $2.54 + 0.44/-0.60$ and β_4 to be $2.29 + 0.07/-0.31$, giving a D to S state mixing of 89% $+3/-12\%$ into the D state with the relative phase angle between the two states being less than 59°. The three-photon generalized cross section is less than 4.4×10^{-79} cm^6 sec^2.

ACKNOWLEDGMENTS

The authors thank L. Collins and S. I. Chu for useful discussions, and G. Vaughn and J. Hontas for technical assistance. Authors from LANL are under Contract No. W-7405-ENG and those from UNM are supported by the Division of Chemical Sciences, Office of Basic Energy Sciences, Office of Energy Research of the U.S. Department of Energy.

[1] H. A. Bethe, Z. Phys. **57**, 815 (1929).
[2] K. R. Lykke, K. K. Murray, and W. C. Lineberger, Phys. Rev. A **43**, 6104 (1991).
[3] Xin Miao Zhao, M. S. Gulley, H. C. Bryant, Charlie E. M. Strauss, David J. Funk, A. Stintz, D. C. Rislove, G. A. Kyrala, W. B. Ingalls, and W. A. Miller, Phys. Rev. Lett. **78**, 1656 (1997).
[4] C. Y. Tang *et al.*, Phys. Rev. Lett. **66**, 3124 (1991).
[5] A. Stintz *et al.*, Phys. Rev. Lett. **75**, 2924 (1995).
[6] J. L. Hall, E. J. Robinson, and L. M. Branscomb, Phys. Rev. Lett. **14**, 1013 (1965).
[7] C. Blondel, M. Crance, C. Delsart, and A. Giraud, J. Phys. B **24**, 3575 (1991).
[8] H. Stapelfeldt, C. Brink, and H. K. Haugen, J. Phys. B **24**, L437 (1991).
[9] L. A. Collins and A. L. Merts, Phys. Rev. A **45**, 6615 (1992).
[10] C. Laughlin and S. I. Chu, Phys. Rev. A **48**, 4654 (1993); further results are given by J. Wang, S. I. Chu, and C. Laughlin, in *ibid.* **50**, 3208 (1994).
[11] C-R. Liu, B. Gao, and A. F. Starace, Phys. Rev. A **46**, 5985 (1992).
[12] D. A. Telnov and S. I. Chu, J. Phys. B **29**, 4401 (1996).
[13] L. A. A. Nikolopoulos and P. Lambropoulos, Phys. Rev. A **56**, 3106 (1997).
[14] I. Sánchez, H. Bachau, and F. Martín, J. Phys. B **30**, 2417 (1997).
[15] C. Blondel and C. Delsart, Nucl. Instrum. Methods Phys. Res. B **79**, 156 (1993).
[16] J. T. Broad and W. P. Reinhardt, Phys. Rev. A **14**, 2159 (1976).
[17] H. C. Bryant and E. P. MacKerrow, in *Accelerator-Based Atomic Physics Techniques and Applications*, edited by Stephen M. Shafroth and James C. Austin (AIP Press, Woodbury, NY, 1997), Chap. 6, pp. 183–214; see also *Atomic and Molecular Physics*, edited by I. Alvarez, C. Cisneros, and T. J. Morgan (World Scientific, River Edge, NJ, 1995), p. 144.
[18] D. Proulx and R. Shakeshaft, Phys. Rev. A **46**, R2221 (1992); further results are given in D. Proulx, M. Pont, and R. Shakeshaft, *ibid.* **49**, 1208 (1994).
[19] H. V. Smith, J. D. Sherman, and P. Allison, CEBAF Report No. 89-001, 1988, p. 164 (unpublished).
[20] Sidney Singer, LALP Report No. 91-1, 1991 (U.S. Government Printing Office: 1991-573-208/20046) (unpublished). A series of staged experiments was planned, leading to a 24 MeV system, and then to a high-energy demonstration. The program was terminated before the 24 MeV accelerator was completed, but the injector with its high brightness ion source and high-voltage power supply was installed in the accelerator hall of the 57 000-square-foot accelerator building.
[21] The BEAR Project (Beam Experiments Aboard a Rocket) is described in Los Alamos National Laboratory Report No. LA-11737-MS, Vol. I, BEAR-DT-7-1 (unpublished).
[22] H. V. Smith, J. D. Sherman, and P. Allison, CEBAF Report No. 89-001, 1988, p. 104 (unpublished).
[23] S. L. Chin, Phys. Rev. A **5**, 2303 (1972).
[24] M. R. Cervenan and N. R. Isenor, Opt. Commun. **13**, 175 (1975).
[25] P. Kruit and F. H. Read, J. Phys. E **16**, 313 (1983).
[26] G. A. Kyrala and T. D. Nichols, Phys. Rev. A **44**, R1450 (1991).
[27] M. S. Gulley, Ph.D. dissertation, University of New Mexico, 1997.
[28] J. Morellec, D. Normand, G. Mainfray, and C. Manus, Phys. Rev. Lett. **44**, 1394 (1980).
[29] M. Edwards and L. Armstrong, J. Phys. B **13**, L497 (1980).
[30] R. Trainham, G. D. Fletcher, and D. J. Larson, J. Phys. B **20**, L777 (1987).
[31] L. Præstegaard, T. Andersen, and P. Balling, Phys. Rev. A **59**, R3154 (1999).
[32] N. C. Barford, *Experimental Measurements: Precision, Error, and Truth* (Addison-Wesley, London, 1967).
[33] M. Crance, Comments At. Mol. Phys. **24**, 95 (1990).
[34] M. Crance, J. Phys. B **21**, 3559 (1988).
[35] C. Blondel, M. Crance, C. Delsart, and A. Giraud, J. Phys. II **2**, 839 (1992).
[36] E. P. Wigner, Phys. Rev. **73**, 1002 (1948).
[37] M. Crance, J. Phys. B **20**, 6553 (1987).